Supporting Information:

A Versatile Self-Assembly Strategy for the Synthesis of Shape-Selected Colloidal Noble Metal Nanoparticle Heterodimers

Tina A. Gschneidtner,[†] Yuri A. Diaz Fernandez,[†] Svetlana Syrenova,[‡] Fredrik Westerlund,[†] Christoph Langhammer,[‡]* Kasper Moth-Poulsen[†]*

[†]*Department of Chemical and Biological Engineering, Chalmers University of Technology, SE-412 96 Göteborg, Sweden*

[‡]*Department of Applied Physics, Chalmers University of Technology, SE-412 96 Göteborg, Sweden*

Contents: page:

SI1 Experimental section

Instruments

SEM: Ultra 55 FEG SEM, Zeiss operated at 10 kV.
TEM: Tecnai T20 LaB6, FEI.
Zeta-Potential and **DLS**: Zetasizer Nano ZS
Centrifuge: Eppendorf Mini Spin rotor KL125 (9 cm)
Dark-field microscope: Nikon Eclipse LV100 with 50x objective, fiber-coupled to a spectrometer Andor Shamrock 303i-B equipped with a CCD camera Andor Newton.

Reagents

All starting materials, including spherical gold and silver nanoparticles (NPs, nominal diameter 100 nm, DLS diameter 90 nm) were purchased from Sigma-Aldrich, and used as received.

Pd and Au nanoparticles of different sizes and shapes were synthetized adapting procedures previously described in the literature.[1–3]

All particles were used fresh, since occasionally sedimentation was observed after several hours. However re-dispersion lead to colloidal solutions, where no reshaping or ripening was reveal by TEM inspection.

Functionalization of NP-A:

NP-A is Au (90 nm) or Ag (90 nm) citrate stabilized NPs, commercially available from Sigma Aldrich. These colloidal solutions were stabilized by adding aliquots of the linker sodium 2-mercaptoethanesulfonate (MESNa) solutions as described below.

<u>Au (90 nm/sphere):</u>

1 ml particle solution ($c_{NP} \approx 3.80 \cdot 10^9$ NP/ml) was mixed with 50 μL of the linker MESNa solution ($6 \cdot 10^{-4}$M). The solution was incubated for 2 h and the excess of linker was removed by centrifugation (3000 rpm, 10 min). The pellet was re-dispersed in 100 μL miliQ water (18MΩ·cm) and therefore a residual concentration of citrate of 30 μM and 3 μM of MESNa remained in the NP solution. The 100 μL NPs were used as they were immediately for dimer formation.

<u>Ag (90 nm/ sphere):</u>

1 ml particle solution ($c_{NP} \approx 8.88 \cdot 10^9$ NP/ml) was mixed with 50 μL of the linker MESNa solution ($6 \cdot 10^{-4}$M). The solution was incubated for 1 h and the excess of linker was then removed by centrifugation (3000 rpm, 10 min). The pellet was re-dispersed in 100 μL miliQ water (18MΩ·cm) and therefore a residual concentration of citrate of 45 μM and 3 μM of MESNa remained in the NP solution. The 100 μL NPs were used as they are immediately for dimer formation.

Synthesis of NP-B:

Au cube (50 nm):

Au nanocubes were synthesized as described elsewhere, the NP concentration was estimated to be $c_{\mathrm{NP}} \approx 1.77 \cdot 10^{11}$ NP/ml.[1] After the synthesis the reaction mixture was centrifuged (6000 rpm, 10 min). The supernatant was removed and the pellet was re-dispersed in 15 ml of miliQ water. To prepare the Au cubes for the dimer synthesis, 1 ml NP (ore more depending on the wanted NP concentration) solution was centrifuged (6000 rpm, 10 min) and the pellet re-dispersed in miliQ water, with a remaining CTAC concentration of 5.8 µM. The 100 µL NPs were used as they are immediately for dimer formation.

Pd cube (20 nm):

Pd 20 nm cubes were synthesized as reported in literature.[2] The NP concentration was estimated to be $c_{\mathrm{NP}} \approx 8.14 \cdot 10^{11}$ NP/ml. The colloidal solutions were store at 30°C for further used.

To prepare these particles for dimer formation 2 or 3 ml of NP solution (depending on the desired concentration) were diluted up to 15 ml with milliQ water. The NPs were centrifuged (8000 rpm, 10 min) and the pellet re-dispersed with 3 µM CTAB solution to 1.5 ml. Centrifuged (6000 rpm, 10 min) and the pellet re-dispersed with 3 µM CTAB solution to 0.5 or 1 ml. Here 75 µL were used for the dimer formation immediately after the centrifugation procedure.

Pd cube (40 nm):

Pd 40 nm cubes were synthesized adapting a method from the literature.[2] The NP concentration was estimated to be $c_{\mathrm{NP}} \approx 2.05 \cdot 10^{10}$ NP/ml. The reaction was terminated by diluting the reaction mixture (5 ml) up to 15 ml with milliQ water and centrifuge it (6000 rpm, 10 min). The pellet was re-dispersed in 5 ml with milliQ water. Prior dimer formation, 1 ml or more (depending on the concentration wanted) was centrifuged (6000 rpm, 10 min) and filled up to 100 µL with 3 µM CTAB solution.

Au rhombic dodecahedral (50 nm):

Au rhombic dodecahedra were synthesized as described before.[1] The NP concentration was estimated to be $c_{\mathrm{NP}} = \approx 6.63 \cdot 10^{10}$ NP/ml. The reaction mixture was centrifuged (6000 rpm, 10 min) and the supernatant removed. The particles were re-dispersed 15 ml (20 µM CTAC). Prior the use for the dimer formation, 1 ml NP (ore more depending on the wanted NP concentration) solution was centrifuged (6000 rpm, 10 min) and the pellet re-dispersed in miliQ water, with a remaining CTAC concentration of 5.8 µM. The 100 µL NPs were used as they were immediately for dimer formation.

Pd truncated cube (130 nm), rhombic dodecahedron (110 nm), octahedron (130 nm)

Different shapes of Pd nanoparticles were synthetized adapting a published versatile synthetic route .[3] The NP concentration was estimated to be $c_{\mathrm{NP,truncated\ cube}} \approx 4.16 \cdot 10^{9}$ NP/ml, $c_{\mathrm{NP,rhombic\ dodecahedral}} \approx 5.4 \cdot 10^{9}$ NP/ml, $c_{\mathrm{NP,octahedron}} \approx 3.59 \cdot 10^{9}$ NP/ml. The reaction was terminated by diluting the reaction mixture (5 ml) up to 15 ml with milliQ water and centrifuge it (6000 rpm, 10 min). The pellet was re-dispersed in 5 ml with milliQ water. For the dimer synthesis, 1 ml (or more depending on the concentration wanted) was centrifuged (6000 rpm, 10 min) and the pellet redispersed in milliQ water to 1 ml. A residual concentration of 4 µM CTAB is remaining.

Self-Assembly of Heterodimers.

The precursor NP-A and NP-B were prepared as described before. In the assembly step it is important to keep the CTAB/CTAC (for NP-B) and citrate (for NP-A) within stability zone described in the main text. The dimers were obtained by mixing 100 µL of functionalized NP-A with 100 µL of precursor NP-B solutions. The amount of NP-A and NP-B in the 100 µL solution was optimized for each dimer combination. The solutions were used immediately after mixing for the preparation of samples for TEM and SEM characterization.

SEM sample preparation

SEM samples were prepared by spin-coating on silicon substrates, previously cleaned with a solution of hydrogenperoxide and sulfuric acid (1:3). The solutions were dropped on the surface immediately after mixing, following a two-step program of 30 s at 1000 and 30 s at 2000 rpm. Samples were analyzed without further modification.

TEM & STM sample preparation

The solutions were drop-cast on copper TEM grids with carbon membranes, and the droplets were immediately allowed to spread and subsequently dry. The solutions were used immediately after mixing as described above.

DLS and Z-potential measurements and sample preparation

For DLS and Z-potential measurements the samples were prepared following the procedures described above for self-assembly experiments. The final volume was adjusted to achieve the minimum volume of solution required for the DLS and Z-potential cells (0.8 ml), keeping the concentrations of surfactants and citrate constant. In the Z-potential experiments, the solutions contained only one kind of particle, and the appropriated concentrations of citrate and cationic surfactants. The hydrodynamic radii were calculated considering the average radius in DLS size-distribution profiles by number of NPs, while direct Z-average values were used to evaluate the presence of large aggregates. In every measurement, the optimal instrument settings lead to reliable data, with good data-quality indicators.

Determiantion of interparticle gap from high magnification TEM imaging

Interparticle distance in self-assembled NP heterodimers was determined using ImageJ. Several TEM images at high magnifications and high contrast were analyzed for each combination of NPs, measuring for each dimeric structure 10 distances in different positions of the gap. The value reported was the average of these measurements. Representative TEM images are presented in SI8.

Single particle scattering-spectra measurement and sample preparation

The samples for dark-field characterization were prepared following the same procedures described above for SEM samples, except for the Si substrates that were thermally oxidized. By combining SEM and dark-field imaging at different magnifications in the same areas of the samples, single heterodimers were identified and their individual scattering spectra were subsequently recorded, using a dark-field microscope (Nikon Eclipse LV100 with 50x objective) fiber-coupled to a spectrometer (Andor Shamrock 303i-B) equipped with a CCD camera (Andor Newton). During dark-field imaging the samples were mounted in a specific cell that allowed the control of the internal atmosphere. Initial spectra of the hetero-dimers were recorded in pure Argon, and then in 80 mbar of hydrogen partial pressure in Argon. The reversibility was tested by measuring the spectra in pure Argon again.

Determination of the mutual stability zone diagram for NP-A ($Au_{90\,nm}$ and NP-B ($Pd_{25\,nm}$)

NP-A and NP-B were synthesized as described above, and the initial concentrations of citrate (30 μM, negatively charged) and CTAB (12.5 mM, positively charged) were as in the synthetic procedures. The own-stabilizer concentrations were then reduced by repeatedly centrifugation and dilution steps, until the desired concentration was achieved. This solutions were then mixed with specific aliquots of the other-stabilizer and the stability could be stablish at naked eye by the loss of color of the solution, indicating bulk aggregation of the colloids. Figures 3 A and B in the main text describe this. The procedure was repeated several times for each own-stabilizer concentration, to establish narrower concentration-windows for the transition point between stable and collapsed colloids.

SI2- Representative STM-EDX analysis of heterodimers

The chemical composition of the NPs forming the hetero-dimers was assayed by STM-EDX analysis at high-magnification. For each heterodimer the EDX spectra was recorded in two areas, each associated with the STM image of each NP (named below Area 1 and 2). The signals for Cu and C from the TEM grid were present in all the samples.

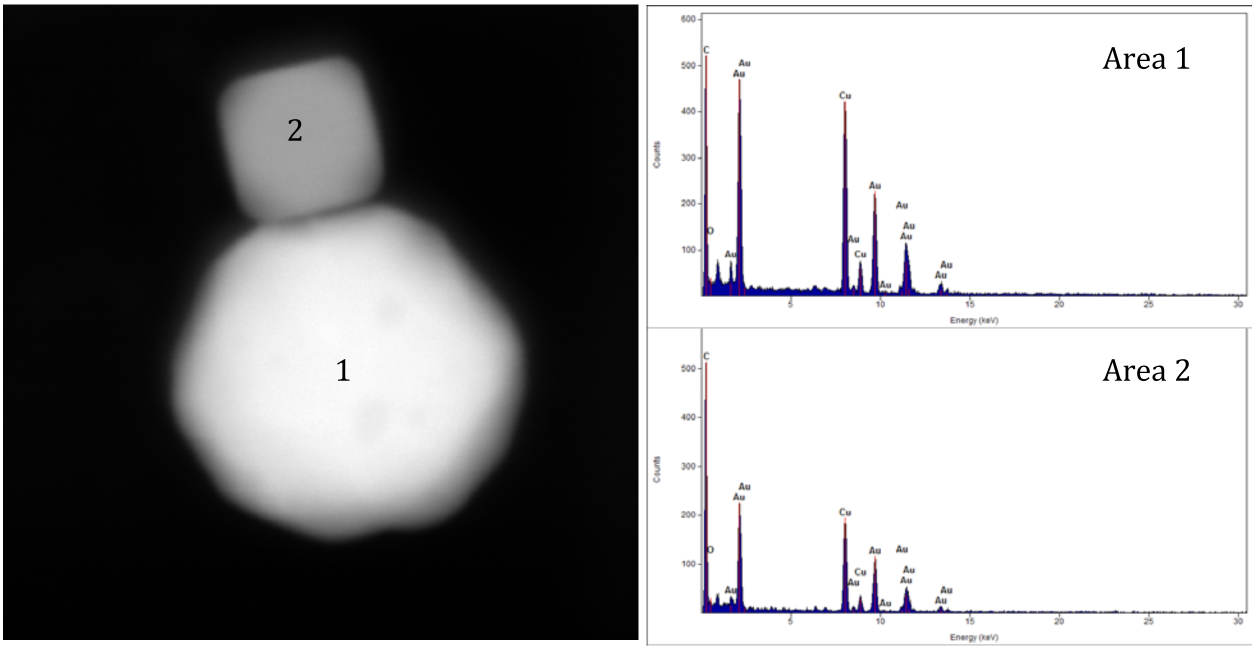

Figure SI2-1. EDX analysis with STEM of the heterodimer Au (spherical, 100 nm) and Au (cube, 50 nm).

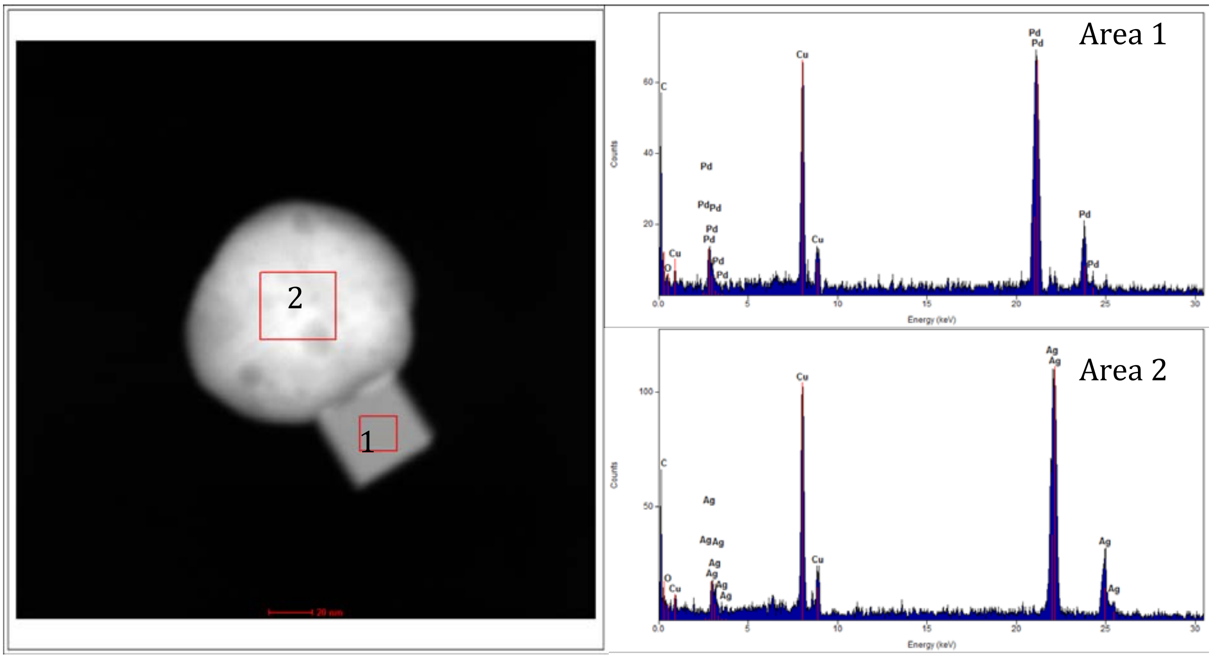

Figure SI2-2. EDX analysis with STEM of the heterodimer Ag (spherical 100 nm) and Pd (cube, 20 nm).

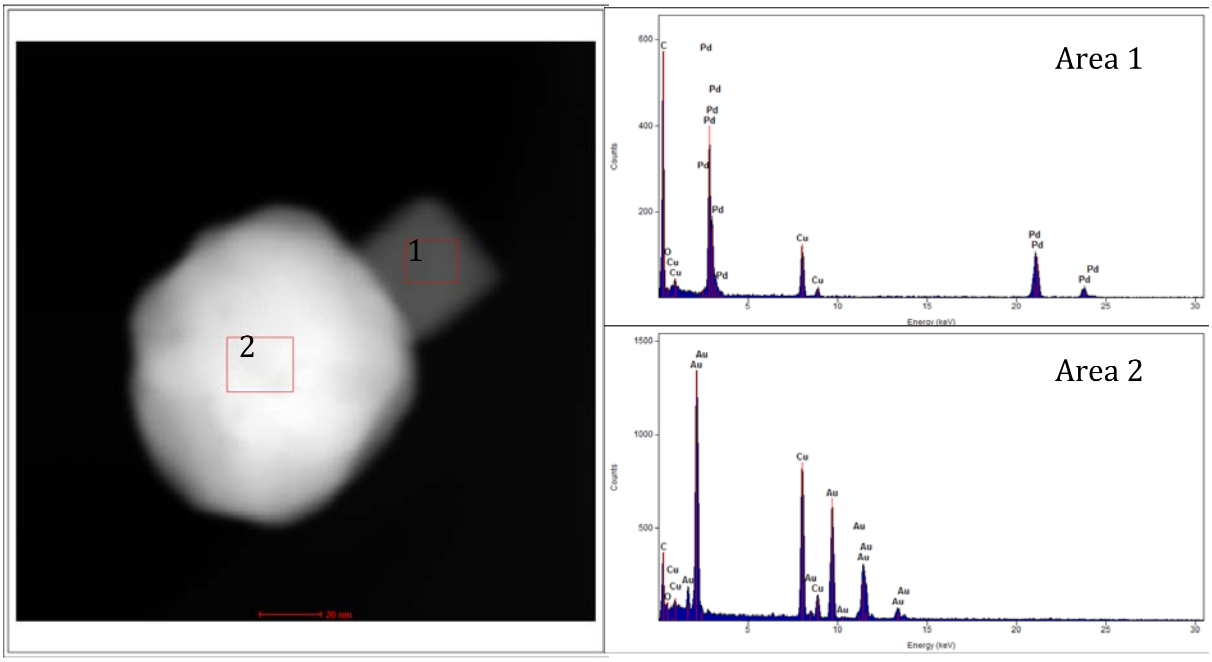

Figure SI2-3. EDX analysis with STEM of the heterodimer Au (spherical 100 nm) and Pd (cube, 20 nm).

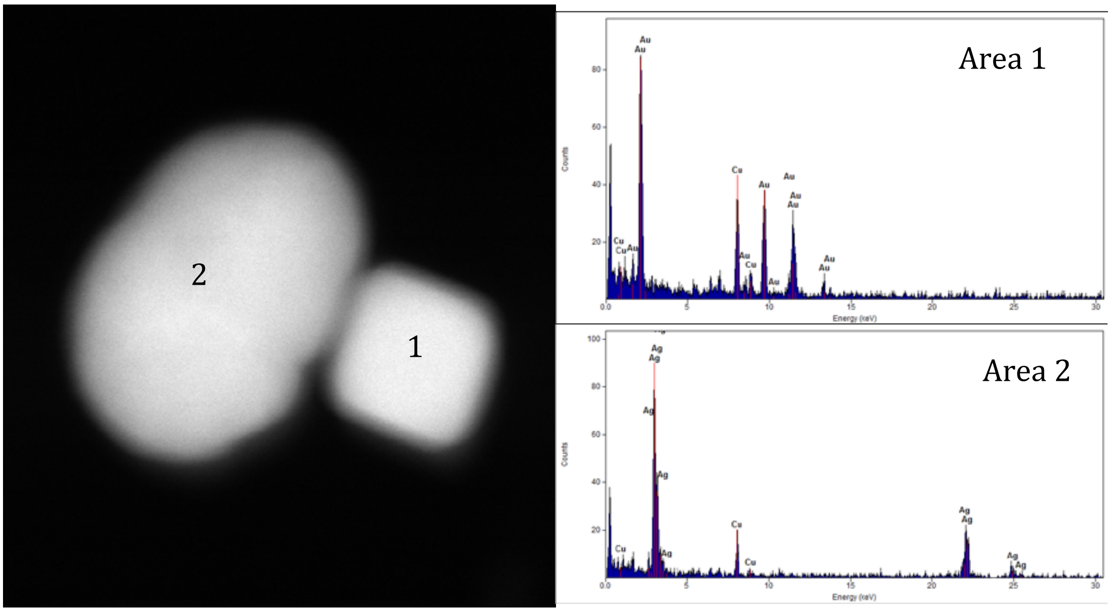

Figure SI2-4. EDX analysis with STEM of the heterodimer Ag (spherical 100 nm) and Au (cube, 50 nm)

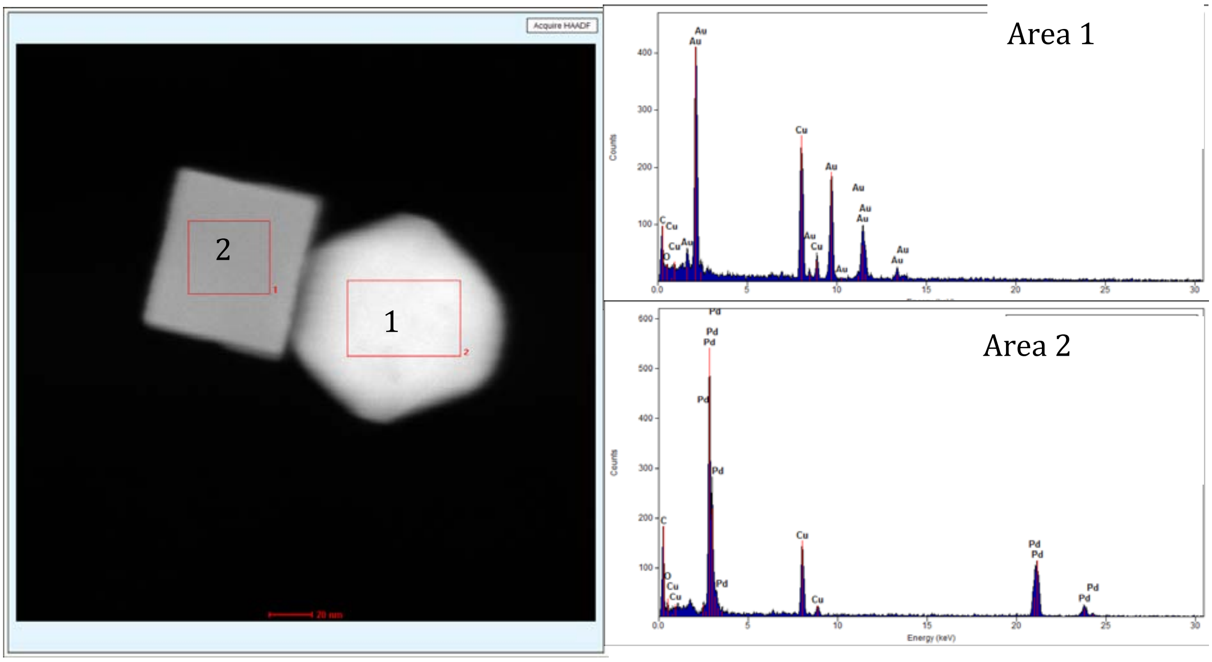

Figure SI2-5. EDX analysis with STEM of the heterodimer Au (spherical, 100 nm) and Pd (40 nm).

SI3 -Representative SEM images of heterodimers solutions deposited on silicon substrates

SEM images for the NP combination Pd cube (25nm) and Au sphere (90nm), showing the composition of the typical data set used in the analysis of the population of aggregates. Dimers are highlighted by circles.

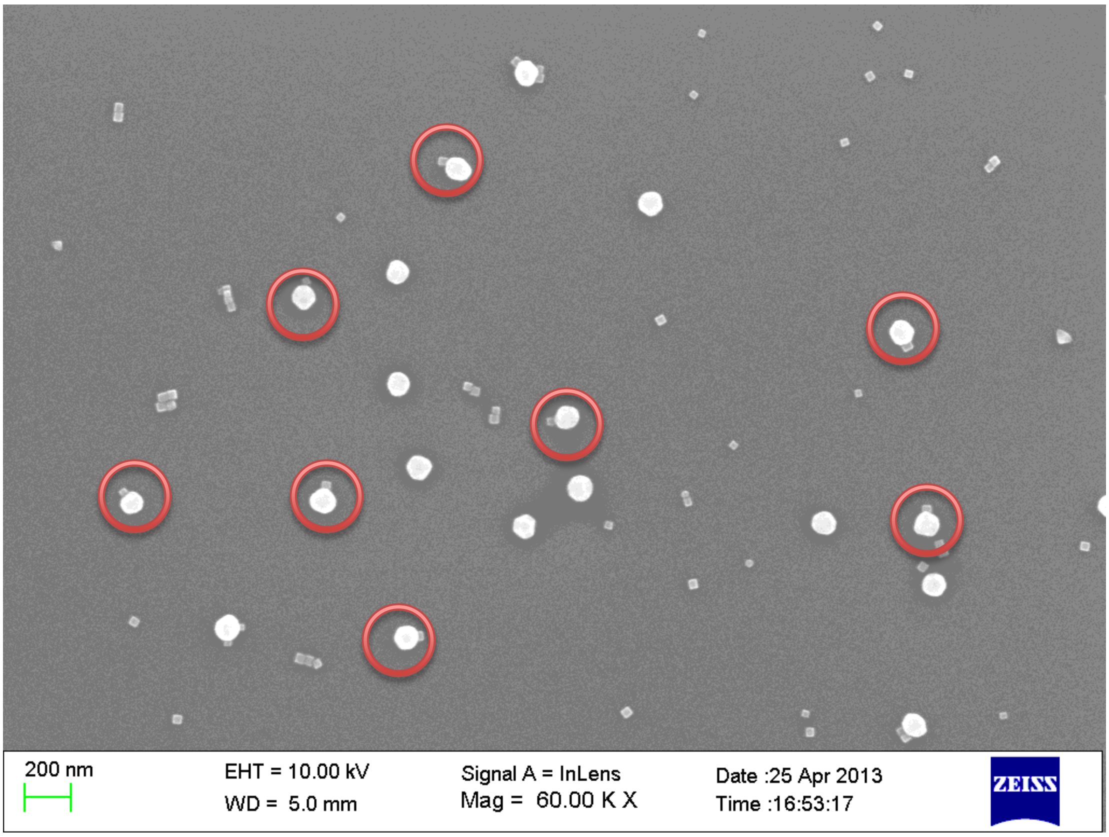

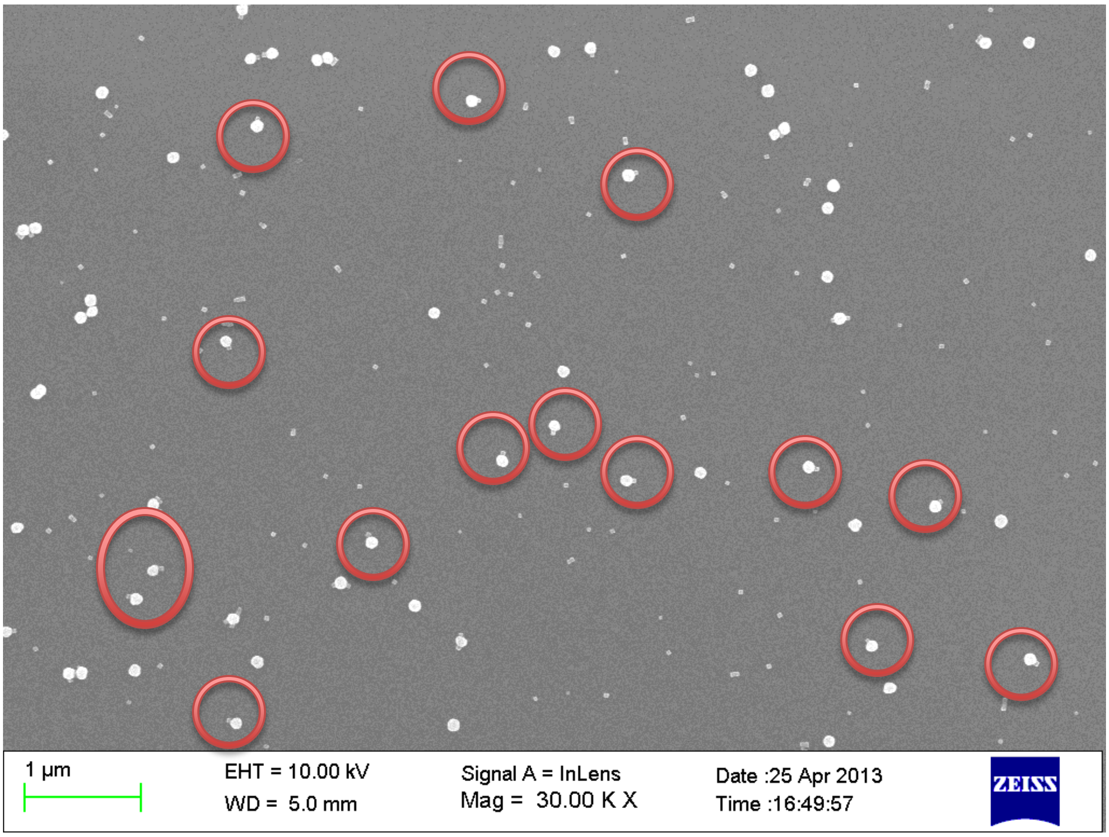

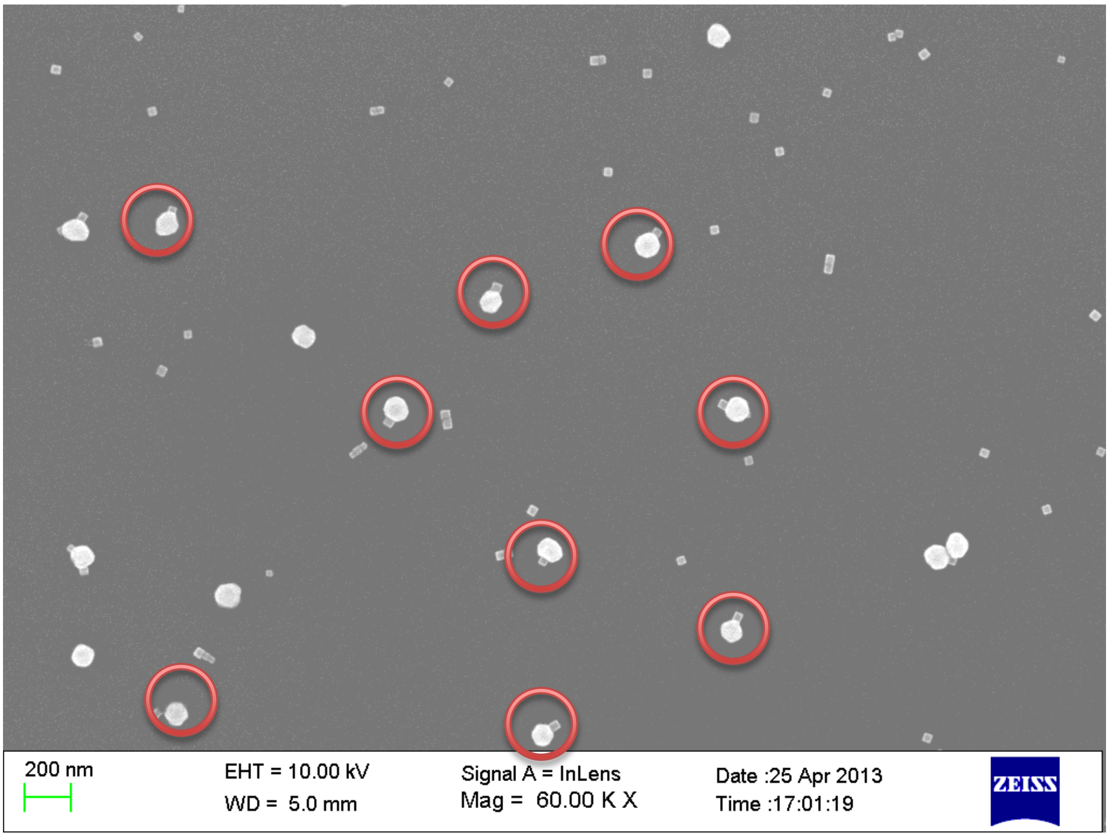
200 nm
EHT = 10.00 kV
WD = 5.0 mm
Signal A = InLens
Mag = 60.00 K X
Date :25 Apr 2013
Time :17:01:19
ZEISS

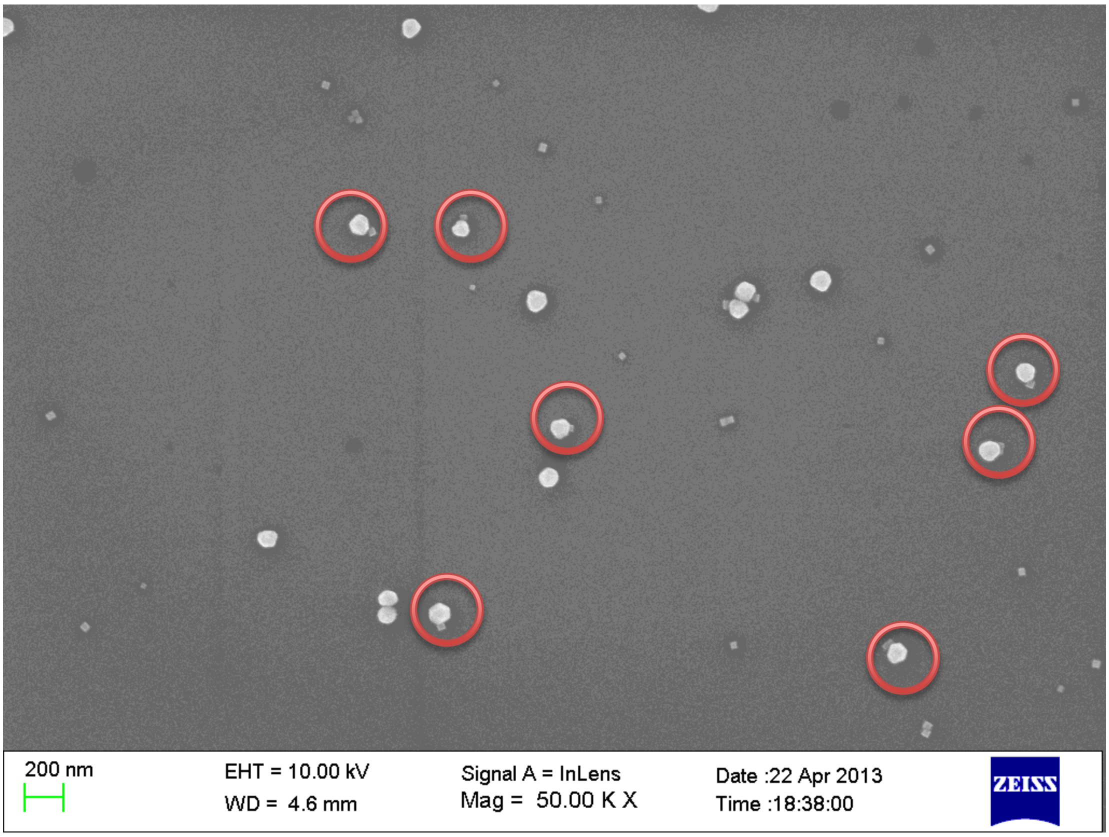
200 nm
EHT = 10.00 kV
WD = 4.6 mm
Signal A = InLens
Mag = 50.00 K X
Date :22 Apr 2013
Time :18:38:00
ZEISS

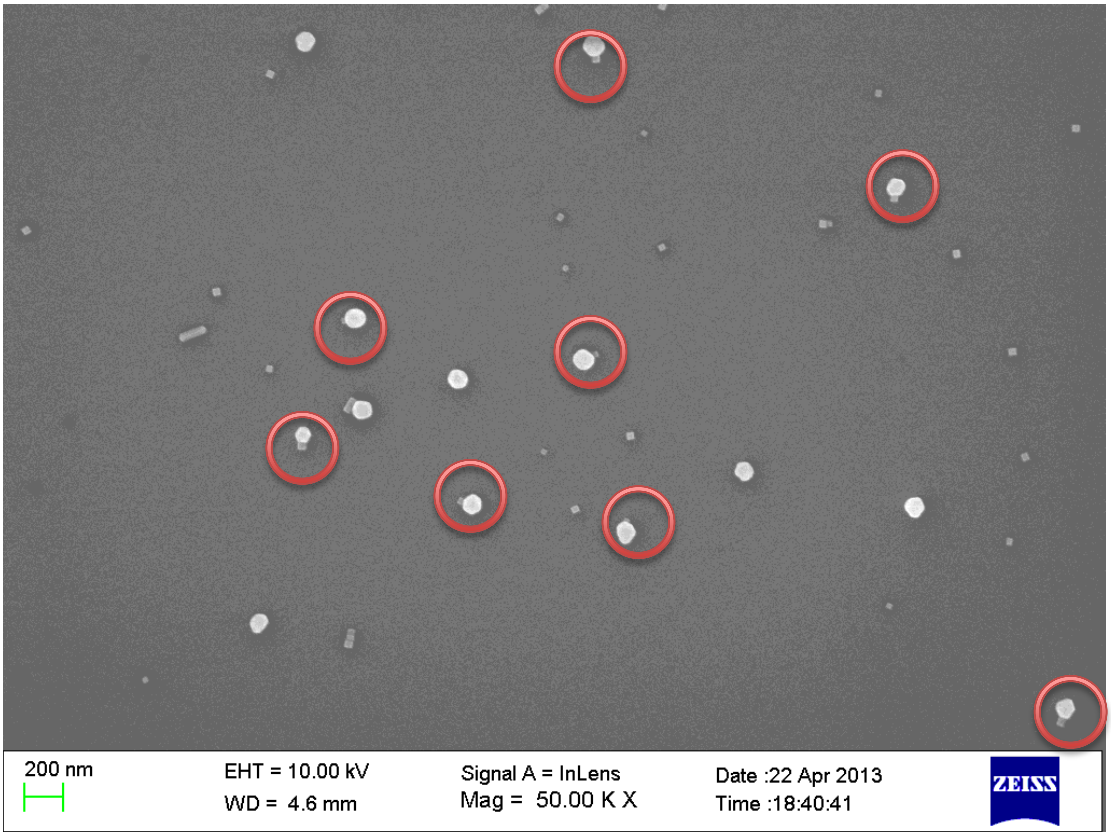
200 nm
EHT = 10.00 kV
WD = 4.6 mm
Signal A = InLens
Mag = 50.00 K X
Date :22 Apr 2013
Time :18:40:41
ZEISS

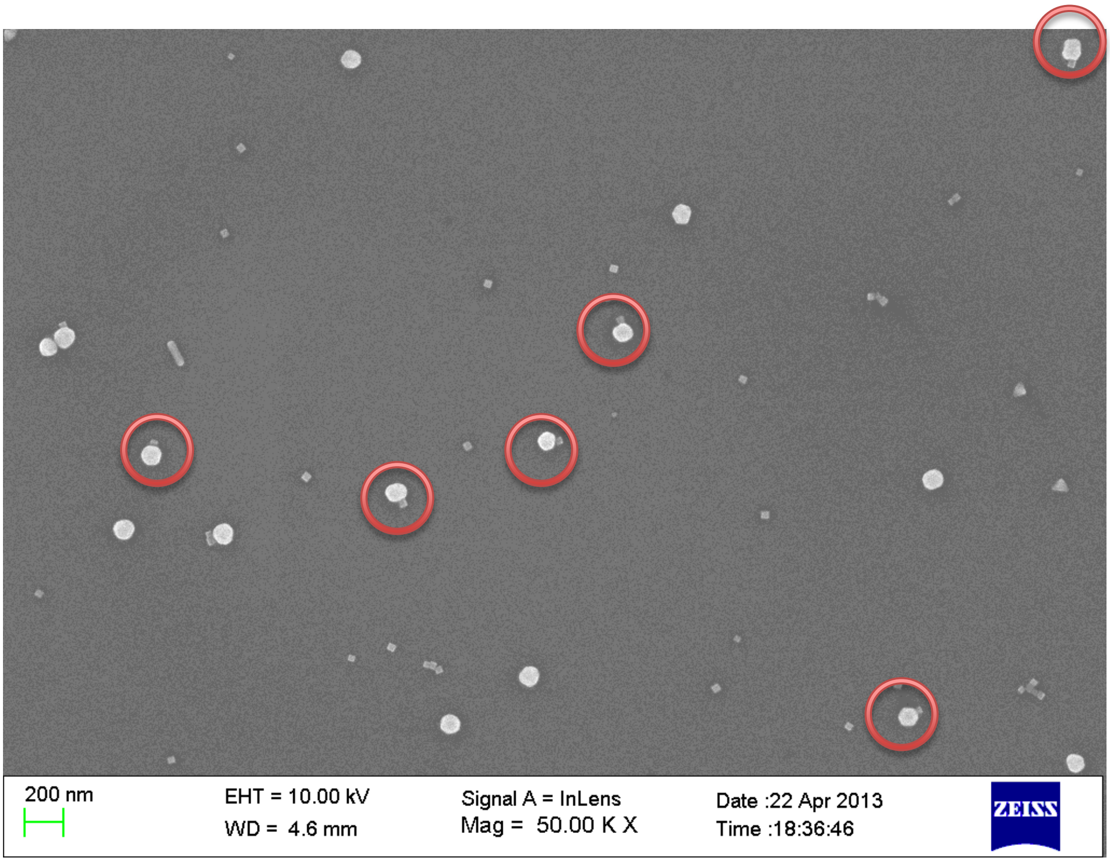
200 nm
EHT = 10.00 kV
WD = 4.6 mm
Signal A = InLens
Mag = 50.00 K X
Date :22 Apr 2013
Time :18:36:46
ZEISS

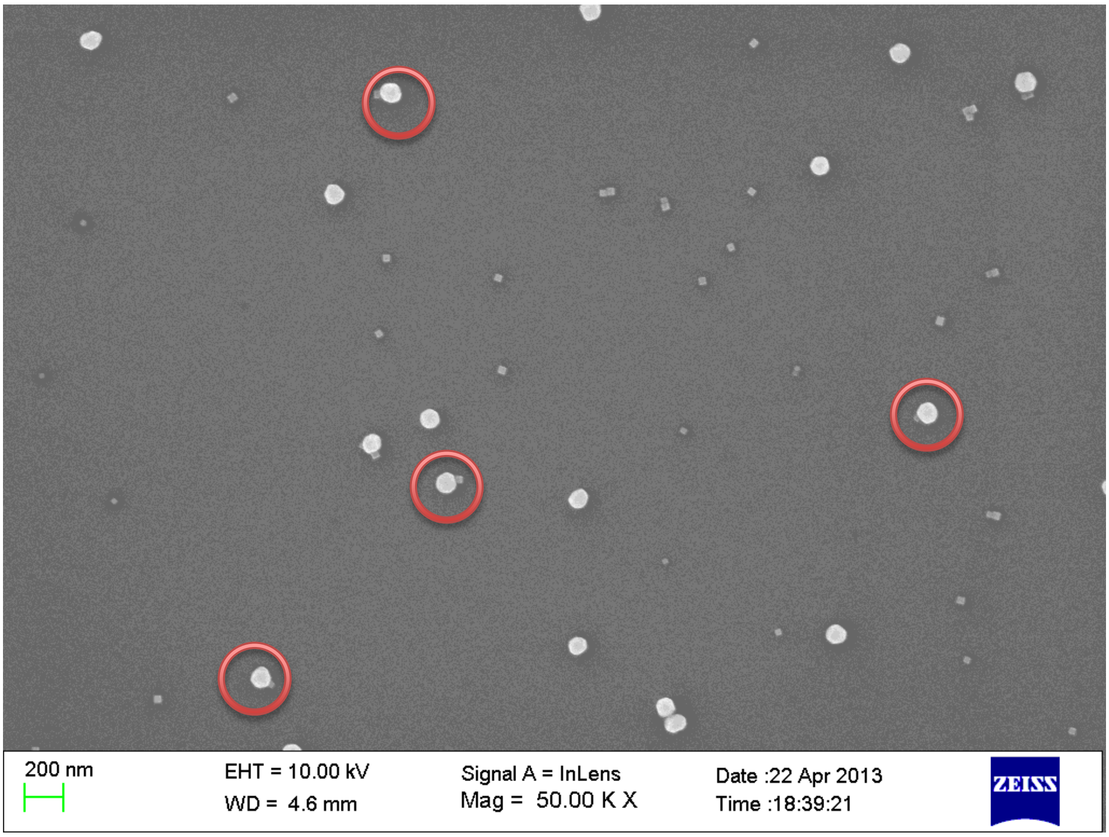
200 nm
EHT = 10.00 kV
WD = 4.6 mm
Signal A = InLens
Mag = 50.00 K X
Date :22 Apr 2013
Time :18:39:21
ZEISS

SI4: Population Statistics of representative nanoparticle combinations

Ag sphere 90 nm – Pd cubes 25 nm:

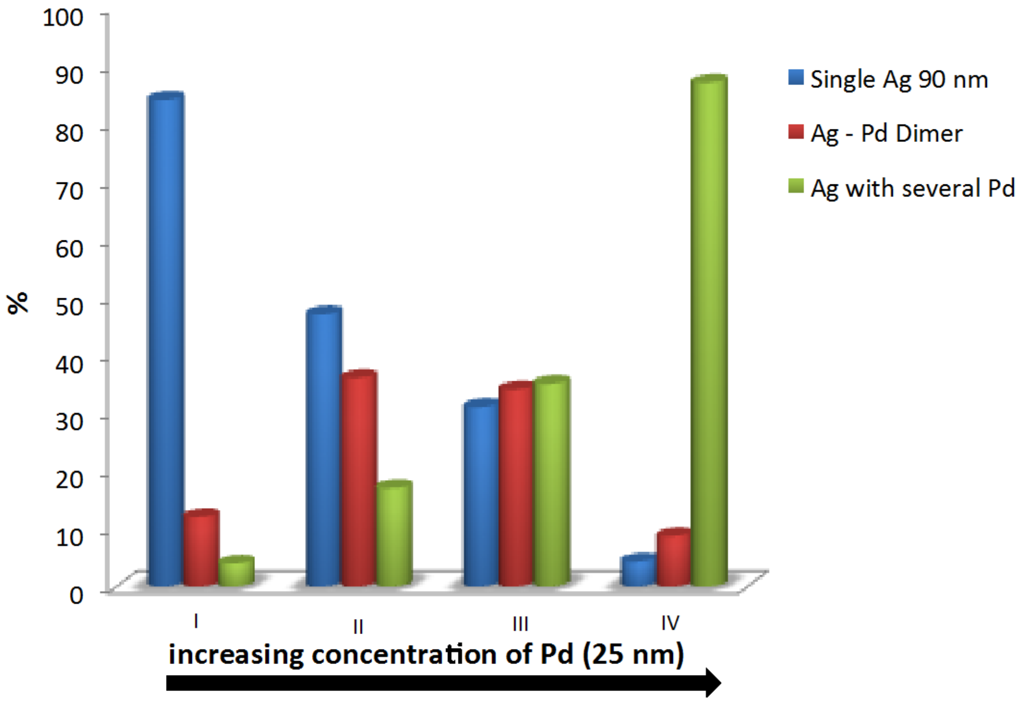

Figure SI4-2. The NP concentrations after combining NP-A and NP-B are: Ag (90 nm), c≈$5.07 \cdot 10^{10}$ NP/ml; Pd 25 nm concentration I: c≈$1.74 \cdot 10^{11}$ NP/ml, II: c≈$6.98 \cdot 10^{11}$ NP/ml, III: c≈$2.44 \cdot 10^{12}$ NP/ml, IV: c≈$2.09 \cdot 10^{12}$ NP/ml.

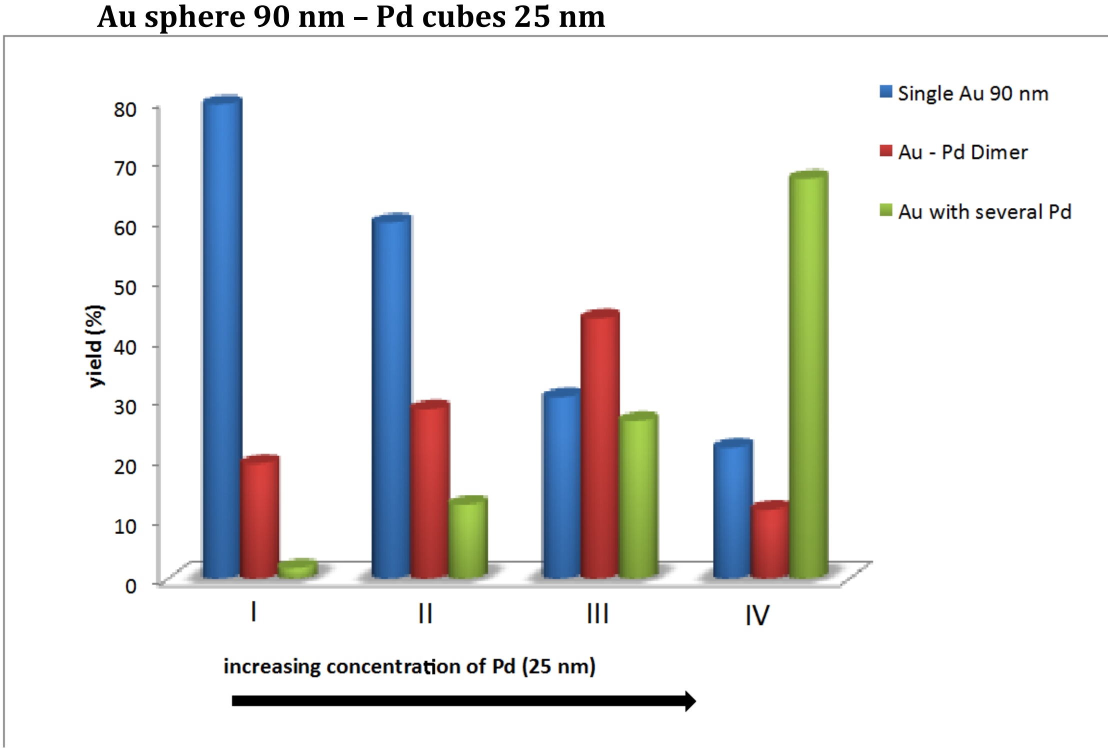

Au sphere 90 nm – Pd cubes 25 nm

Figure SI4-3. The NP concentrations after combining NP-A and NP-B are: Au (90 nm), c≈$2.17 \cdot 10^{10}$ NP/ml; Pd 25 nm concentration I: c≈$3.49 \cdot 10^{11}$ NP/ml, II: c≈$6.98 \cdot 10^{11}$ NP/ml, III: c≈$1.40 \cdot 10^{12}$ NP/ml, IV: c≈$2.09 \cdot 10^{12}$ NP/ml.

Au sphere 90 nm – Au cubes 35 nm

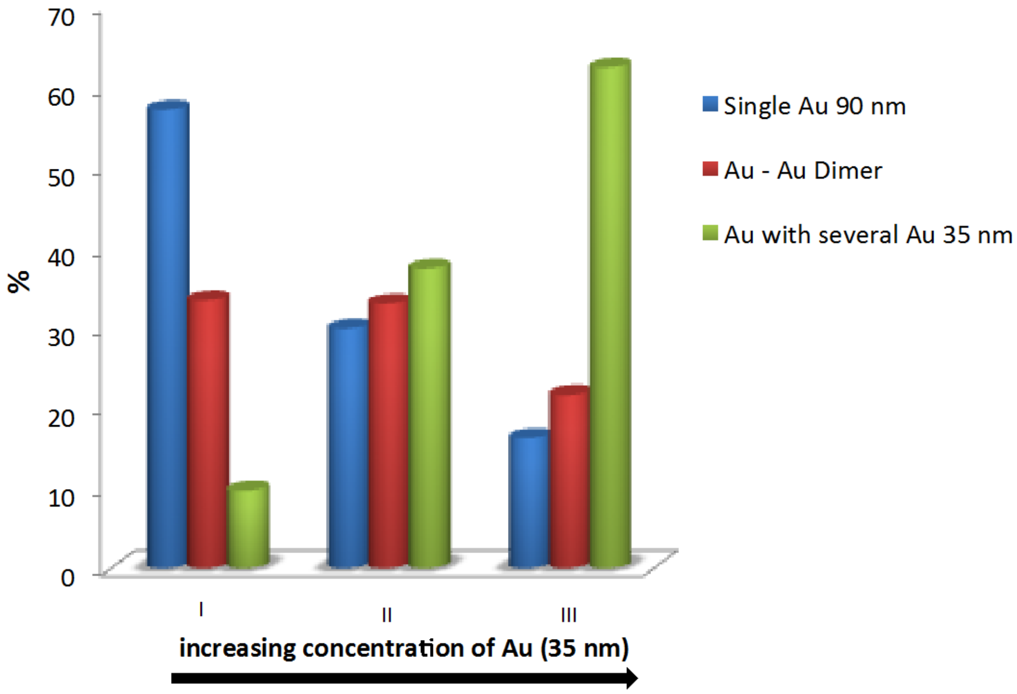

Figure SI4-4. The NP concentrations after combining NP-A and NP-B are: Au (90 nm), $c \approx 9.5{\cdot}10^{9}$ NP/ml; Au 35 nm concentration I: $c \approx 8.60{\cdot}10^{10}$ NP/ml, II: $c\approx 2.15{\cdot}10^{11}$ NP/ml, III: $c\approx 4.30{\cdot}10^{11}$ NP/ml.

Ag sphere 90 nm – Au cubes 35 nm

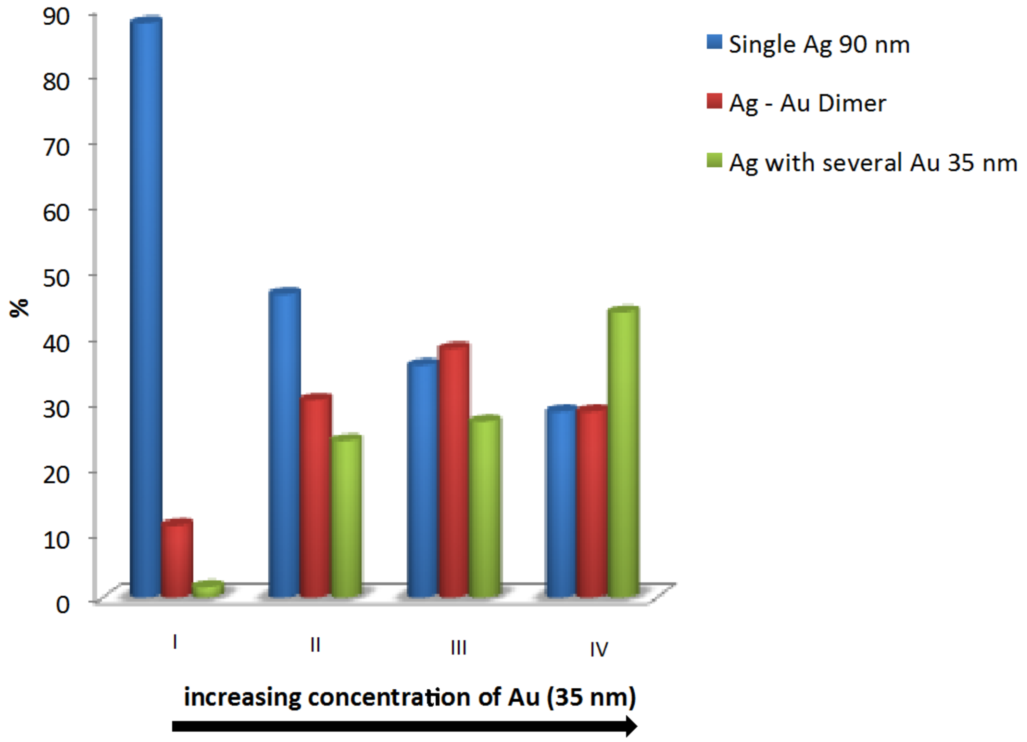

Figure SI4-5. The NP concentrations after combining NP-A and NP-B are: Ag (90 nm), c≈$2.22 \cdot 10^{10}$ NP/ml; Au 35 nm concentration I: c≈$8.60 \cdot 10^{10}$ NP/ml, II: c≈$2.15 \cdot 10^{11}$ NP/ml, III: c≈$4.30 \cdot 10^{11}$ NP/ml, IV: c≈$1.61 \cdot 10^{12}$ NP/ml.

Au sphere 90 nm – Pd cubes 70 nm

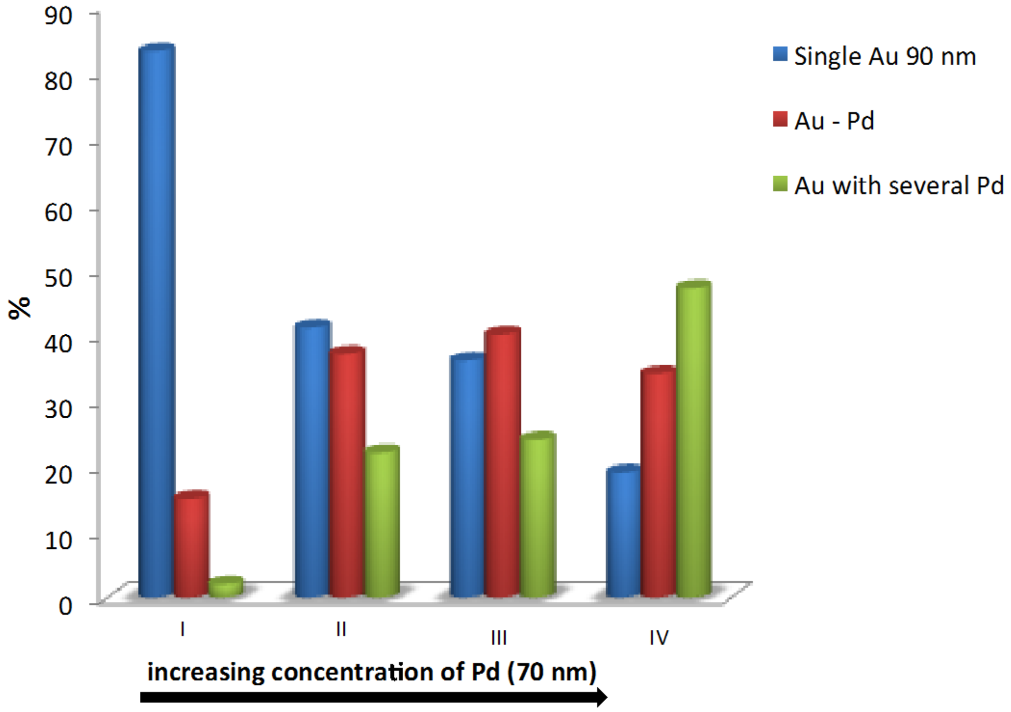

Figure SI4-6. The NP concentrations after combining NP-A and NP-B are: Au (90 nm), $c \approx 1.90 \cdot 10^{10}$ NP/ml; Pd 70 nm concentration I: $c \approx 1.03 \cdot 10^{11}$ NP/ml, II: $c \approx 3.08 \cdot 10^{11}$ NP/ml, III: $c \approx 4.10 \cdot 10^{11}$ NP/ml, IV: $c \approx 6.15 \cdot 10^{11}$ NP/ml.

SI5-A) Zeta-Potential of Au (90 nm) NP (NP-A) as a function of CTAB concentration

An increase of the concentration of a positively charged surfactant (CTAB) decreases the absolute value of the zeta-potential of the negatively charged Au-NP. Lower absolute values of zeta potential indicate less stable Au-NP in solution. In these experiments different aliquots of CTAB stock-solution were added to the Au-NP colloid. The measurements were performed at 35 °C with a thermal equilibration time of 2 min. The shown data are the average of three independent measurements.

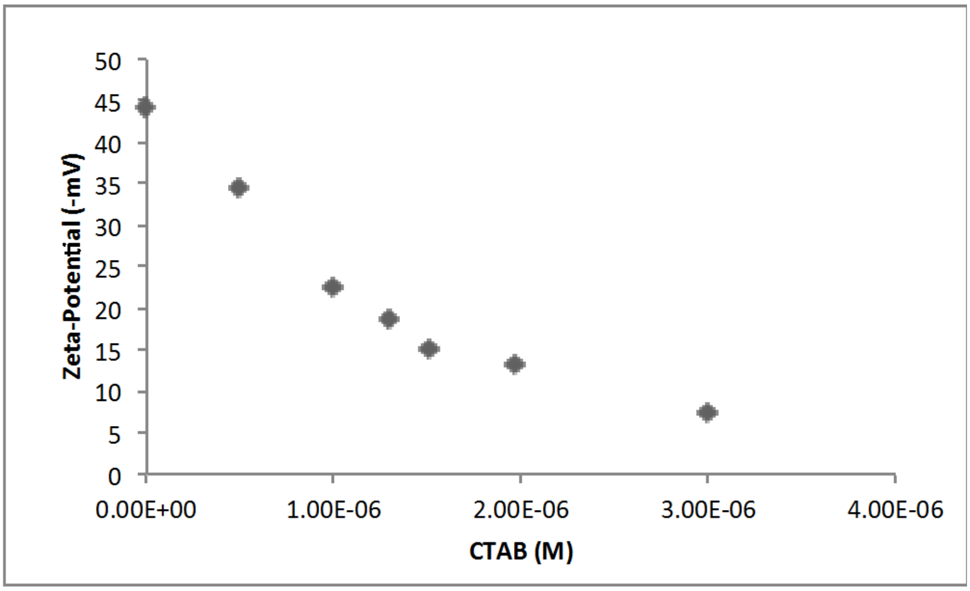

SI5-B) Zeta-Potential of Pd (25 nm) NP (NP-B) as a function of tri-sodium citrate concentration

The zeta-potential of palladium (25 nm, cubic) NP decreases while increasing the concentration of tri-sodium citrate in solution. Therefore the stability of the NPs also decreases.

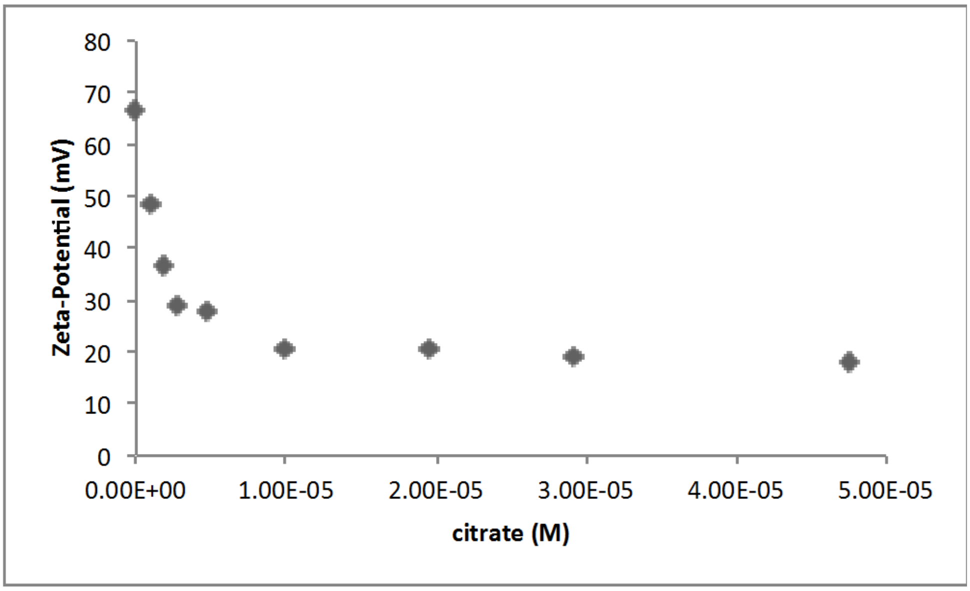

SI6: DLS cumulant zeta-average data of representative dimer combinations and its starting NP`s

NP	Zeta-average (nm)	PdI
Ag sphere 90 nm	116 (1)	<0.09
Au sphere 90 nm	112 (1)	<0.05
Pd cube 70 nm	98 (1)	<0.09
Au rhombic octahedral 50 nm	79 (1)	<0.14
Au cube 35 nm	47 (1)	<0.2
Au (90 nm)- Pd (70 nm)	104 (1)	<0.07
Ag (90 nm)- Au (35 nm)	108 (1)	<0.15
Au (90 nm)- Au (50 nm)	99 (1)	<0.13

The cumulant zeta-average does not significantly increase during the self-assembly experiments, suggesting that the formation of large aggregates in solution can be ruled out.

SI7. Theoretical considerations.

SI7.1 Interaction potential between NPs.

The interaction energy between two nanoparticles A and B (NPs) can be divided into three contributions[4–6] :

$$V_T^{AB} = V_{elec}^{AB} + V_{VdW}^{AB} + V_{solv}^{AB} \qquad \text{Eq. SI1}$$

For spherical NPs, the van der Waals contribution V_{VdW}^{AB} can be expressed as a function of the center-to-center distance (R):

$$V_{VdW}^{AB} = -\frac{A_H^{AB}}{6}\left(\frac{2r_A r_B}{R^2-(r_A+r_B)^2} + \frac{2r_A r_B}{R^2-(r_A-r_B)^2} + ln\left[\frac{R^2-(r_A+r_B)^2}{R^2-(r_A-r_B)^2}\right]\right) \qquad \text{Eq. SI2}$$

Where r_A and r_B are the radii of the nanoparticles, and A_H^{AB} is the Hamaker constant (*e.g.* A_H^{AB} for gold is 2.5 x 10^{-19} J).[6]

The solvation repulsion potential (V_{solv}) is a short range interaction that depends on the solvent decay lengths (*l*), and can be written as follow:

$$V_{solv}^{AB} = \pi A_s l \left[\frac{2r_A r_B}{r_A+r_B}\right] e^{-\frac{R-(r_A+r_B)}{l}} \qquad \text{Eq. SI3}$$

A_s is a pre-exponential factor (1.5 x 10^{-3} J/m^2), and the exponential decay $l = 10^{-9}$ m.[5]

The electrostatic contribution V_{elec}^{AB} can be estimated by the approximation proposed by Ohshima[7]. Under our experimental conditions, the ionic strength is controlled by the concentration of tri-sodium citrate in solution, leading to the inverse Debye-length $\kappa = 1.95 \times 10^7$ m^{-1}, that satisfies the applicability condition of Ohshima's approximation ($\kappa \cdot r_i < 5$) for all the particles investigated here (representative $\kappa \cdot r_i$ values are presented in table SI7-1). In this approximation, the interaction between two spherical colloidal particles (V_{elec}^{AB}) can be expressed as a function of the scaled effective surface potentials of the particles (Y_i):

$$V_{elec}^{AB} = 4\pi\epsilon_s\epsilon_0 r_A r_B \left(\frac{k_B T}{z_e}\right)^2 Y_A Y_B \frac{e^{-\kappa[R-(r_A+r_B)]}}{R} \qquad \text{Eq. SI4}$$

In this expression ε_S is the relative dielectric constant of the solvent, ε_0 is the electric permittivity of vacuum, k_B is Boltzmann's constant, T is temperature, and z_e is the elemental charge of the electron. The scaled effective surface potentials (Y_i) are defined by the set of equations:

$$Y_i = \psi_i^S e^{\int_0^{\psi_i^S}\left[\frac{1}{F_i(y)}-\frac{1}{y}\right]dy} \qquad \text{Eq. SI5}$$

$$F_i(y) = \frac{\kappa r_i}{\kappa r_i+1} g(y)\left[1 + \frac{2(2\kappa r_i+1)}{g^2(y)\,(\kappa r_i)^2}\int_0^y g(u)du\right]^{1/2} \qquad \text{Eq. SI6}$$

$$g(u) = \frac{\psi_i^s}{|\psi_i^s|}\sqrt{\frac{2\sum_{k=1}^{N} n_k(e^{-z_k u}-1)}{\sum_{k=1}^{N} z_k^2 n_k}} \qquad \text{Eq. SI7}$$

Where ψ_i^s is the scaled surface potential of particle i, having surface potential ψ_i at temperature T:

$$\psi_i^s = \frac{z_e \psi_i}{k_B T} \qquad \text{Eq. SI8}$$

In Eq. SI7, it is implicitly assumed that the solution contains a completely-dissociated electrolyte, and the summation includes the ions of charge z_k and stoichiometric coefficient n_k. Considering a 1:3 electrolyte (i.e. tri-sodium citrate, which is the salt that dominates the ionic strength in the self-assembly experiments), equation 7 can be written:

$$g(u) = \frac{\psi_i^s}{|\psi_i^s|}\sqrt{\frac{1}{6}(e^{3u} + 3e^{-u} - 4)} \qquad \text{Eq. SI9}$$

It can be inferred from Eq. SI9 that g(u) has the same sign as ψ_i^s, and the factorization of the term under the root indicates that g(u) takes real values for any value of u. The set of equations SI5, SI6, and SI9 can be solved by numerical integration for specific values of ψ_i^s and κr_i, leading to the scaled effective surface potentials for each type of NP (Y_i), that can be substituted in Eq. SI4 to calculate the electrostatic interaction energy as a function of interparticle distance (Representative profiles are presented in Figure SI7 – 1).

Preliminary inspection of equations SI2 to SI9 suggests that the nature of the material composing the NPs and the properties of the solvent have a direct effect on the entity of the interactions, as well as the size of the NPs involved. Moreover, the ionic strength (defining the value of κ) and the surface potential of the NPs (ψ_i) are crucial, determining whether the electrostatic interaction is repulsive ($\psi_A\psi_B > 0$) or attractive ($\psi_A\psi_B < 0$). Since van der Waals interactions are strong at short range and attractive until NP-AP contact, the electrostatic potential energy results in a long range driving force for formation of aggregates for NPs of different kinds (hetero-aggregates), or generates an energetic barrier for aggregation of NPs of the same kind (homo-aggregates).

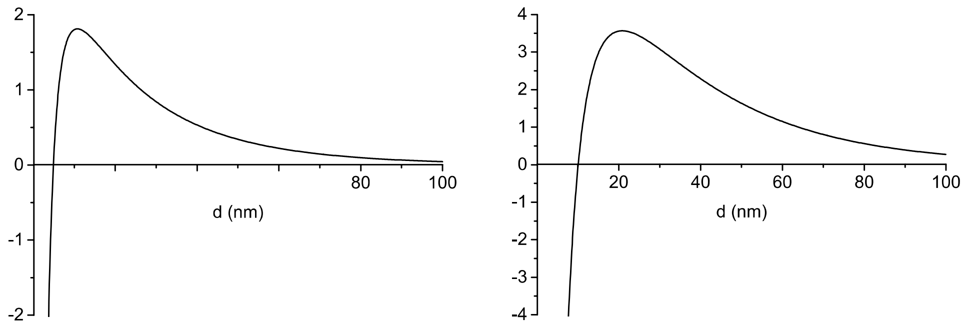

Figure SI7-1. Interaction energy vs interparticle separation for representative :) homodimer Au sphere$_{90nm}$ with Au sphere$_{90nm}$; D) multimer Pd cube$_{25nm}$ with different Au sphere$_{90nm}$ - Pd cube$_{25nm}$ (AB$_n$) multimers. The legend in) describes the composition of the multimers considering one NP A (Au sphere$_{90nm}$) and different numbers of B (Pd cube$_{25nm}$). (same as Figure 4 in main text, showed here for didactical reasons)

The experimental stability phase diagram (discussed in the main text) can be quantitatively understood in term of the interaction energy involved in self-aggregation. We have observed that CTAB induced massive self-aggregation in MESNa functionalized Au NPs (NP-A) and concluded that destabilization can be associated to reduction of the Z-potential of the NPs in the presence of the cationic surfactant. The reduction of Z-potential induces a decrease in the energy barrier for self-aggregation, and when this barrier is below the thermal energy, the NPs irreversibly aggregate (selected data illustrating this effect is presented in Figure SI7-2). It is therefore possible to correlate the transition line in the stability phase diagram of the NPs to the concentration of CTAB reducing the self-aggregation energy barrier below k_bT, and consequently causing the collapse of the colloidal solution. In the experimental conditions used for the self-assembly experiments, this maximum allowed CTAB concentration is 2 μM. On the other hand, the minimum concentration of CTAB needed to stabilized Pd cube$_{25nm}$ is around 0.5 μM, therefore the concentration zone in which both kinds of NPs are stable is very narrow, and precise control of surfactant concentration must be achieved to obtained controlled self-assembly. Similar results have obtained for the self-aggregation energy barrier of Pd cube$_{25nm}$ as a function of citrate concentration (Figure SI7-2c,d), by using the appropriate expression for the mixed electrolyte solution Citrate/CTAB in Eq. SI9.[7] Under the experimental conditions for the self-assembly experiments the concentration of citrate that reduces the repulsion barrier for self-aggregation to thermal energy is 30 μM. Combining these theoretical results with the stability experiments, we can confirm that the concentration of both capping agents should be carefully tuned to guarantee mutual stability of the two NP types combined by electrostatic self-assembly.

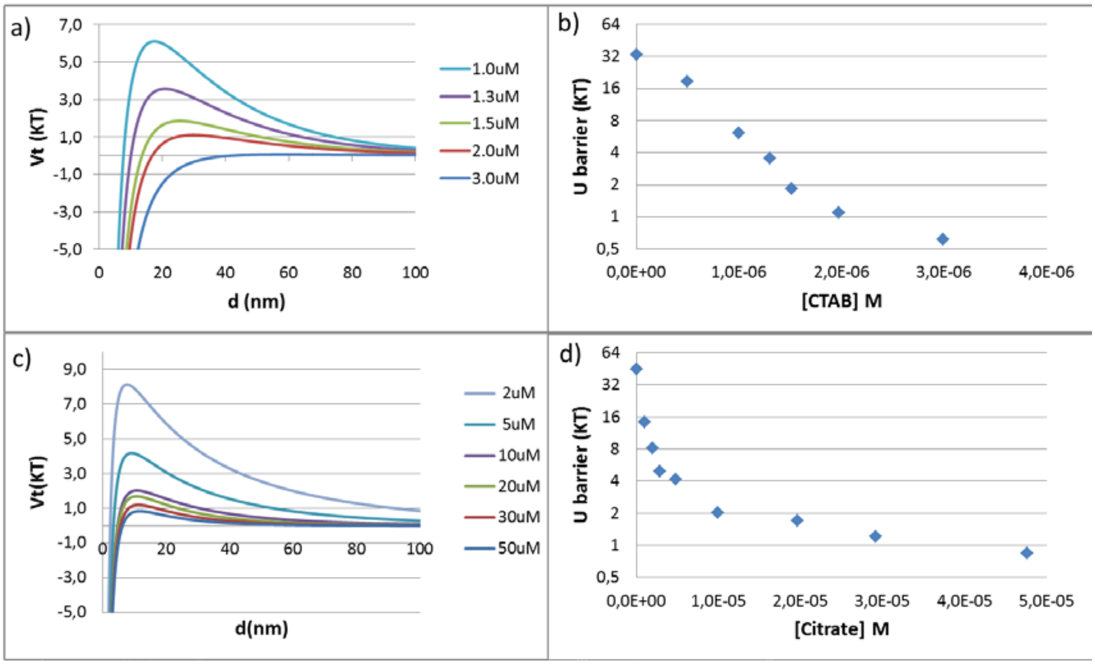

Figure SI7-2. a) Calculated self-aggregation energy (Vt) as a function of interparticle distance for Au sphere$_{90nm}$ at different CTAB concentrations (as described in the legend); b) self-aggregation energy barrier vs CTAB concentration for Pd cube$_{25nm}$; c) Calculated self-aggregation energy (Vt) as a function of interparticle distance for Pd cube$_{25nm}$ at different CTAB concentrations (as described in the legend); d) self-aggregation energy barrier vs CTAB concentration for Pd cube$_{25nm}$;

On the other hand, the formation of multimers (aggregates with several NPs) can be understood considering a step-wise aggregation process, that for low NPs concentrations describes the kinetic mechanism accurately, since 3-bodies (and higher order) simultaneous collisions can be neglected. Under these conditions, the energetic driving force for the formation of a multimer of type AB_{n+1} can be attributed to the pair-wise interaction energy of the multimer AB_n with B. The major challenge in this formulation is the complexity of the interaction potential generated by AB_n. We have considered AB_n as the corresponding sphere of effective radius $<r>_n$ and corresponding surface potential $<\psi>_n$ determined by the equations:

$$\langle r\rangle_n = \sqrt[3]{r_A^3 + n\, r_B^3} \qquad \text{Eq. SI10}$$

$$\langle \psi\rangle_n = \frac{r_A\, \psi_A + n\, r_B\, \psi_B}{\langle r\rangle_n} \qquad \text{Eq. SI11}$$

Eq. SI10 can be obtained straight forward from geometrical considerations, while Eq. SI11 was derived from Ohshima's expression for the surface potential as a function of the surface charge.[8]

By substitution of $<r>_n$ and $<\psi>_n$ in equations SI1 to SI9, the pair-interaction energy profiles as a function of interparticle distance can be calculated for different AB_n multimers interacting with one B particle (Figure SI7-1d). The electrostatic interactions multimer-B are attractive for low B-occupancy numbers (A, AB, AB_2, and AB_3) but becomes repulsive if the number of B in the multimer is larger than 3. The change in sign of $<\psi>_n$ generates an energy barrier that becomes higher than the thermal energy for occupancy numbers larger than 4. Therefore, we can conclude that the formation of multimers with large number of NP-B is energetically disfavored, and the yield of such structures is expected to be low. This theoretical result is consistent with the interpretation of the self-assembly experiments and DLS data discussed in the main text.

A similar approach can be applied to the general multimers A_mB_n, but we have limited our analysis to aggregates containing only one NP-A, since the energy barrier-repulsion for A-A is at least twice the barrier of B-B (for the case of Au $\text{sphere}_{90\text{nm}}$ and Pd $\text{cube}_{25\text{nm}}$), therefore self-aggregation of NPs A is disfavored. This consideration also explains the experimental observation of low yields for A_mB_n multimers with m>1, and justifies the calculation of the statistic populations based on NP-A (further discussion is presented in the main text).

We have extended the model discussed above for Au $\text{sphere}_{90\text{nm}}$ and Pd $\text{cube}_{25\text{nm}}$ to the other combinations of NPs investigated here. The theoretical results suggest that, under our experimental conditions, the energy barriers for self-aggregation disfavor the formation of homodimers (Table SI7-1), while for hetero-aggregation the interactions are attractive, and provide the driving force for the preferential formation of hetero-aggregates under controlled experimental conditions.

Table SI7-1 Simulation parameters for the interaction in homodimers: hydrodynamic radii <r>, scaled radii κ<r>, zeta-potential Ψ, scaled surface potential ψ^s, Ohshida's effective scaled surface potential Y, self-aggregation energy barrier $U_{barrier}$, interparticle distance at maximum energy d_{max}.

NP	<r> (nm)	κ<r>	Ψ (mV)	ψ^s	Y	$U_{barrier}$ (k_bT)	d_{max} (nm)
Au_{sphere}	46	1.42	-18.6	-0.724	-0.646	3.57	21
Ag_{sphere}	45	1.38	-18.3	-0.713	-0.610	2.91	22
Pd_{cube1}	13	0.42	20.6	0.802	0.710	1.59	11
Pd_{cube2}	35	1.09	20.3	0.790	0.673	3.44	18
Pd_{rhomb}	55	1.69	36.3	1.413	0.977	14.67	15
Pd_{octa}	63	1.95	21	0.817	0.668	4.80	23
Pd_{trunc}	60	1.84	24	0.934	0.741	6.63	20
Au_{cube}	18	0.55	30	1.168	0.951	5.22	10
Au_{rhomb}	25	0.77	30	1.168	0.930	6.58	12

SI7.2 Relative abundance of aggregates

In the presence of irreversible aggregation, the formation of NP aggregates can be related to the collision rates depending on the NP interaction energy and on the cross-section of collision. Attractive interactions (like in hetero-aggregates) will increase the frequency of collisions, while repulsive forces (like in homo-aggregates) will reduce the collisional rate. Considering the dilute regime (*i.e.* long interparticle distances), the fluctuating Brownian diffusion will be altered by the permanent interparticle forces, delaying aggregation for the same kind of NPs, and promoting the formation of hetero-aggregates. If we consider that this driving force for aggregation has an effective radius of action R_a, and assuming that the average distance between two NP of type A is larger than R_a, we can infer that the n particles B within a distance R_a from one particle A will lead to formation of an aggregate of type AB_n. Under these considerations, the probability of formation of the cluster AB_n among the populations of clusters

{AB$_k$} can be related to the probability ($\hat{P}_{AB_n}$) of finding n particles B in the effective action volume of one NP-A (v_a) defined by the radius of action R$_a$. In the dilute regime, this probability can be described by a Poisson distribution[9]:

$$\hat{P}_{AB_n} = \frac{([B]\cdot v_a)^n}{n!}\, e^{-([B]\cdot v_a)} \qquad \text{Eq. SI12}$$

It is interesting to notice that the quantity $[B]\cdot v_a$ defines the average number of NPs B in the effective volume of action v_a, and the Poisson distribution accounts for the fluctuations of the occupancy number within the volume $v_a$under equilibrium conditions. Consequently, summation of $\hat{P}_{AB_n}$ over all n-values is equal to 1.

The probabilities for the single NP-A (n=0), for the dimers AB (n=1), and for the multimers (AB$_n$, n>1) can be written following Eq. SI12 as:

$$\hat{P}_A = e^{-([B]\cdot v_a)} \qquad \text{Eq. SI13}$$

$$\hat{P}_{AB} = ([B]\cdot v_a)\, e^{-([B]\cdot v_a)} \qquad \text{Eq. SI14}$$

$$\hat{P}_m = 1 - (\hat{P}_A + \hat{P}_{AB}) \qquad \text{Eq. SI15}$$

From Eq. SI13 and Eq. SI15, we can conclude that the fraction of single NP-A decays monotonously with the concentration of B, while the fraction of AB has a maximum for $[B] = 1/v_a$. The effective volume of action depends on the entity of the interaction forces between the particles, on the mutual diffusion rate, and on the time of incubation. For the combinations of NPs investigated here, we have estimated the effective interaction volume under our experimental conditions, from the plot of $-\ln(\hat{P}_A)$ vs the concentration of NP-B, following Eq. SI15 (Figure SI7-2d, 3d, 4d). The slopes of these plots gives directly v_a for each combination of NPs under the specific experimental conditions for the self-assembly experiments.

We have calculated the theoretical population compositions at different concentrations of NP-B for representative combinations of NPs (Fig. SI7-3 to 7) using the values of v_a obtained. The theoretical data is in good agreement with the experimental values; especially for low concentrations of NP-B, suggesting that the fluctuation model discussed above describes the trends on the populations of single, dimeric, and multimeric NPs properly for the combinations of NPs investigated in this work.

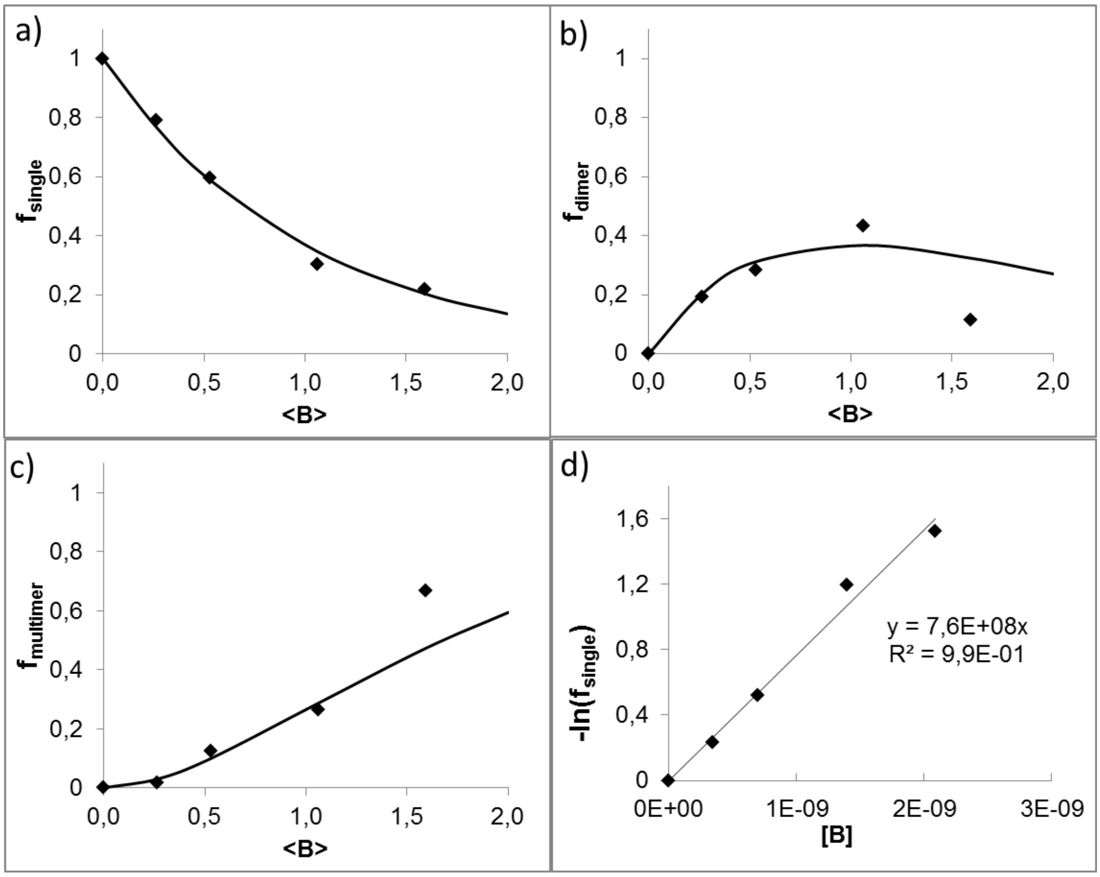

Figure SI7-3. Experimental (dots) and theoretical (lines) population relative abundance for a) single Au sphere$_{90nm}$, b) heterodimers Au sphere$_{90nm}$ - Pd cube$_{25nm}$, c) multimers Au sphere$_{90nm}$ - Pd cube$_{25nm}$; as a function of the average number of Pd cube$_{25nm}$ in the effective volume of action of Au sphere$_{90nm}$; and plotting for the determination of the effective volume of interaction from the experimental data on single A. [B] is the concentration of NP-B expressed in NP/nm^3. The inset equation describes the best fitting line.

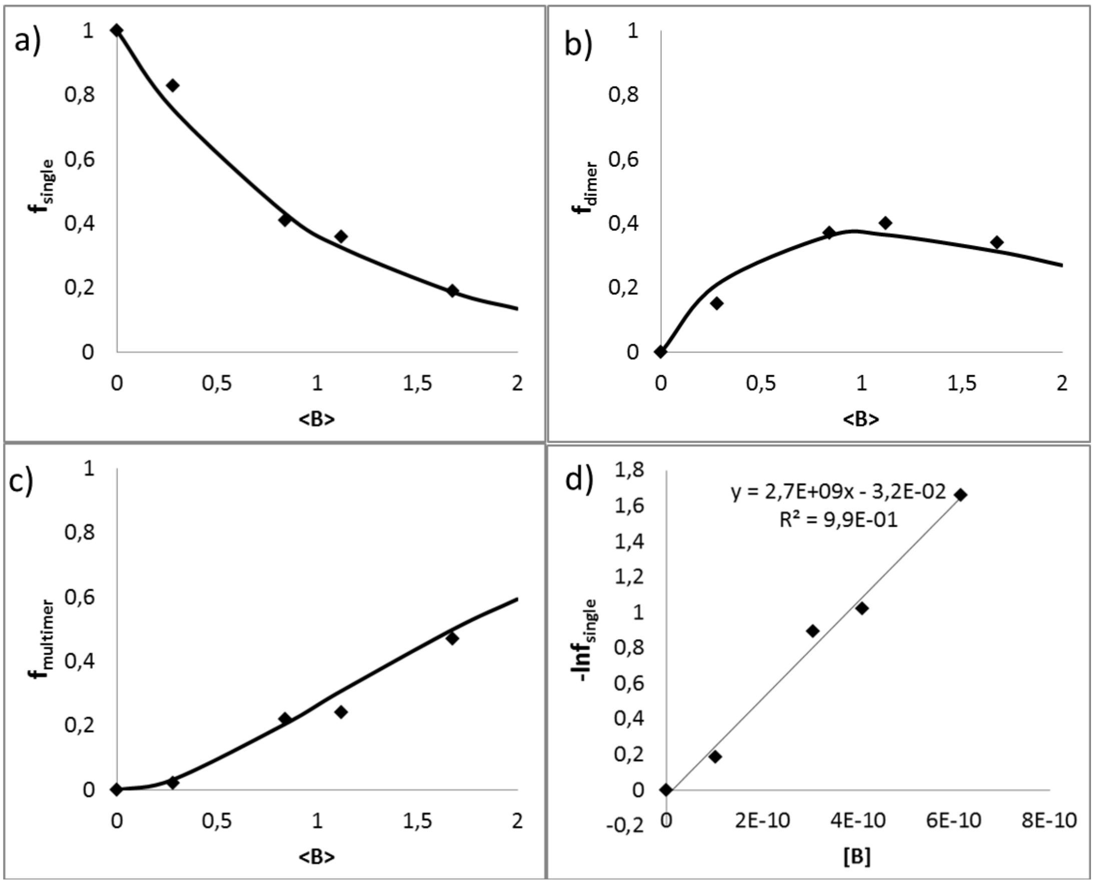

Figure SI7-4. Experimental (dots) and theoretical (lines) population abundance for a) single Au sphere$_{90nm}$, b) heterodimers Au sphere$_{90nm}$ - Pd cube$_{70nm}$, c) multimers Au sphere$_{90nm}$ - Pd cube$_{70nm}$; as a function of the average number of Pd cube$_{70nm}$ in the effective volume of action of Au sphere$_{90nm}$; and plotting for the determination of the effective volume of interaction from the experimental data on single A. [B] is the concentration of NP-B expressed in NP/nm^3. The inset equation describes the best fitting line.

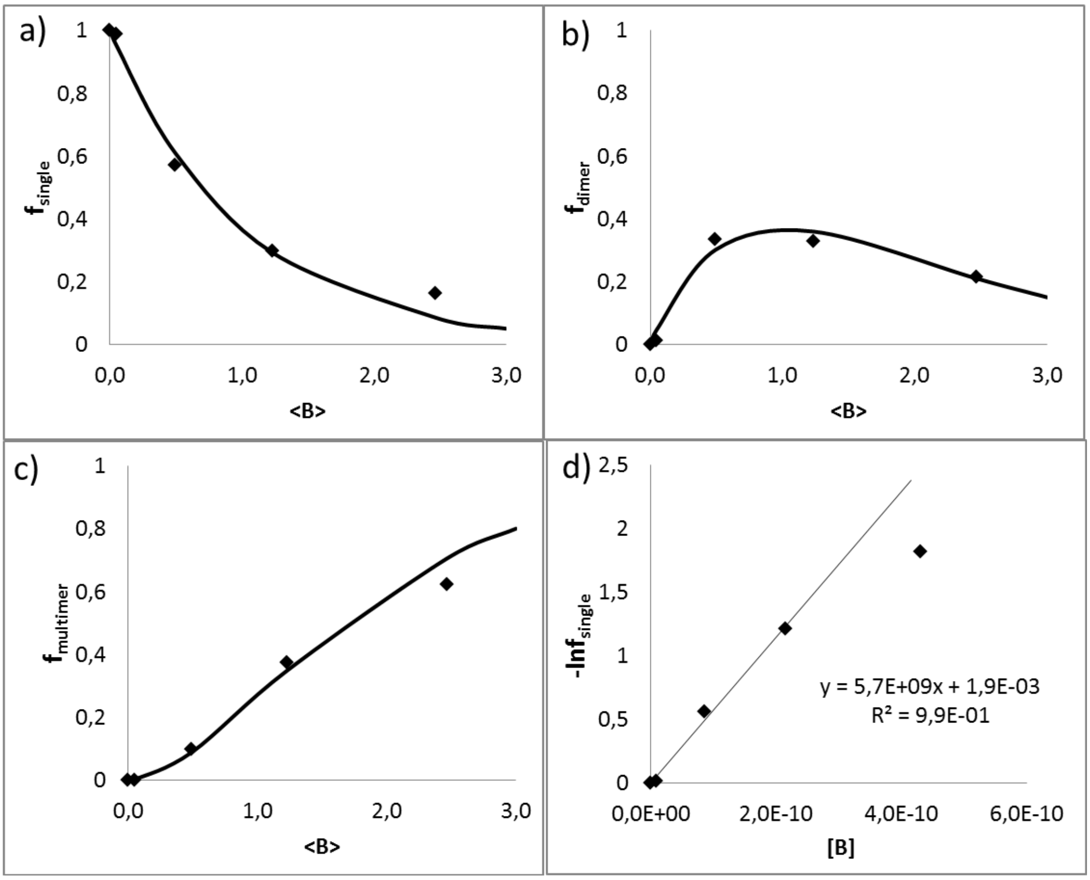

Figure SI7-5. Experimental (dots) and theoretical (lines) population relative abundance for a) single Au sphere$_{90nm}$, b) heterodimers Au sphere$_{90nm}$ - Au cube$_{36nm}$, c) multimers Au sphere$_{90nm}$ - Au cube$_{36nm}$; as a function of the average number of Au cube$_{36nm}$ in the effective volume of action of Au sphere$_{90nm}$; and plotting for the determination of the effective volume of interaction from the experimental data on single A. [B] is the concentration of NP-B expressed in NP/nm^3. The inset equation describes the best fitting line.

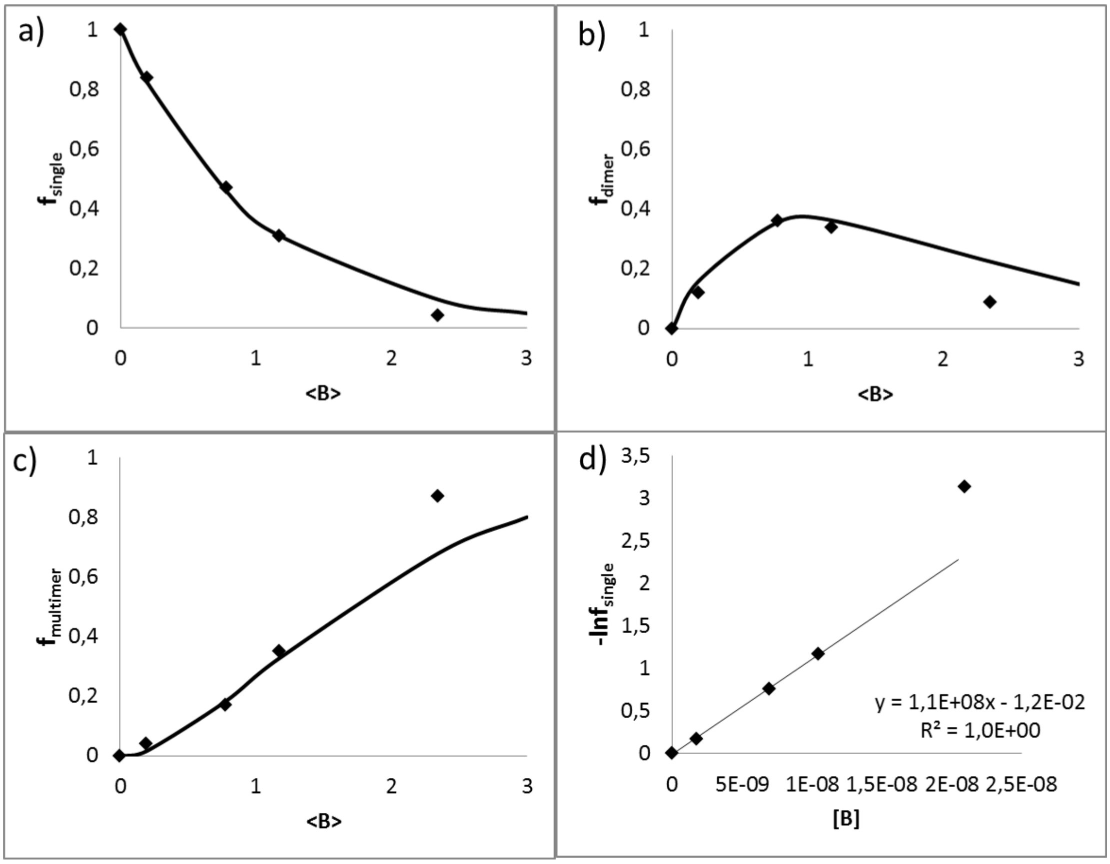

Figure SI7-6. Experimental (dots) and theoretical (lines) population relative abundance for a) single Ag sphere$_{90nm}$, b) heterodimers Ag sphere$_{90nm}$ - Pd cube$_{25nm}$, c) multimers Ag sphere$_{90nm}$ - Pd cube$_{25nm}$; as a function of the average number of Pd cube$_{25nm}$ in the effective volume of action of Ag sphere$_{90nm}$; and plotting for the determination of the effective volume of interaction from the experimental data on single A. [B] is the concentration of NP-B expressed in NP/nm^3. The inset equation describes the best fitting line.

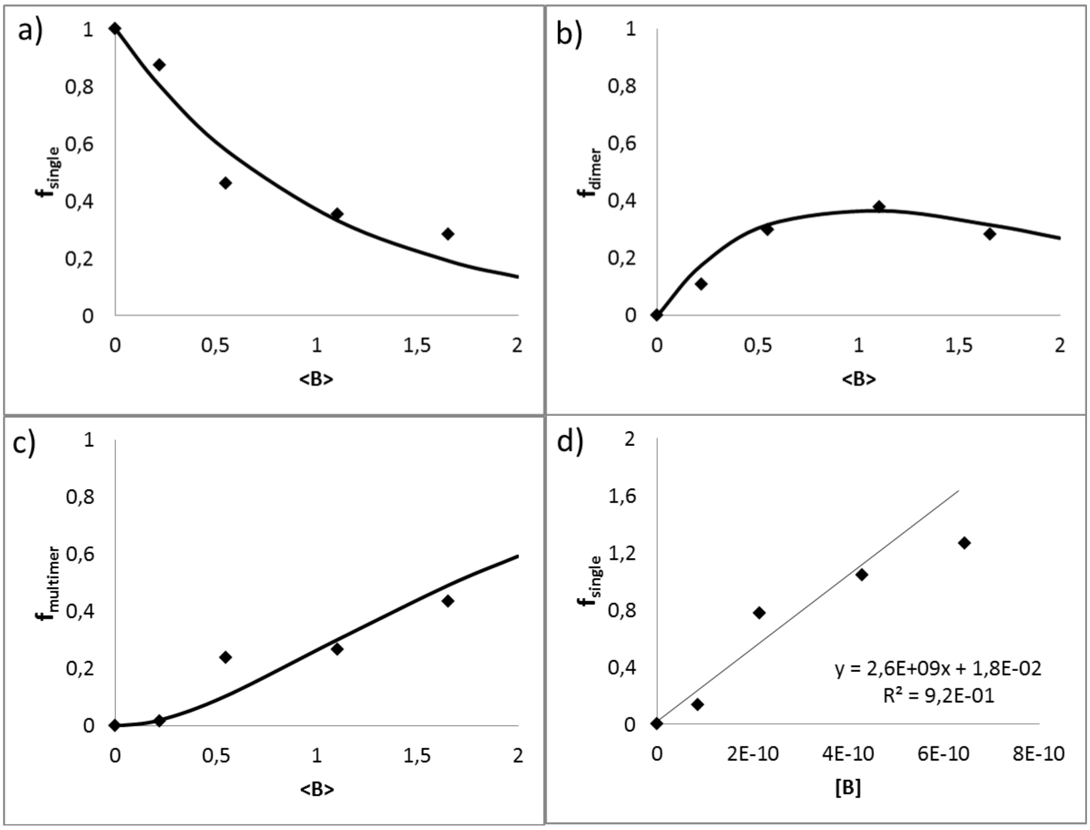

Figure SI7-7. Experimental (dots) and theoretical (lines) population relative abundance for a) single Ag sphere$_{90nm}$, b) heterodimers Ag sphere$_{90nm}$ - Au cube$_{36nm}$, c) multimers Ag sphere$_{90nm}$ - Au cube$_{36nm}$; as a function of the average number of Au cube$_{36nm}$ in the effective volume of action of Ag sphere$_{90nm}$; and plotting for the determination of the effective volume of interaction from the experimental data on single A. [B] is the concentration of NP-B expressed in NP/nm^3. The inset equation describes the best fitting line.

SI-8: TEM imaging of interparticle gap in Heterodimeric Structures

For the determination of the sizes for interparticle gaps between two NPs forming a heterodimer, several heteroaggregates of the same NPs combination were analyzed using high magnification TEM. Each gap was measured at several spots, and the gap size lies between 0.8 nm and 1.9 nm as an average for all heterodimers.

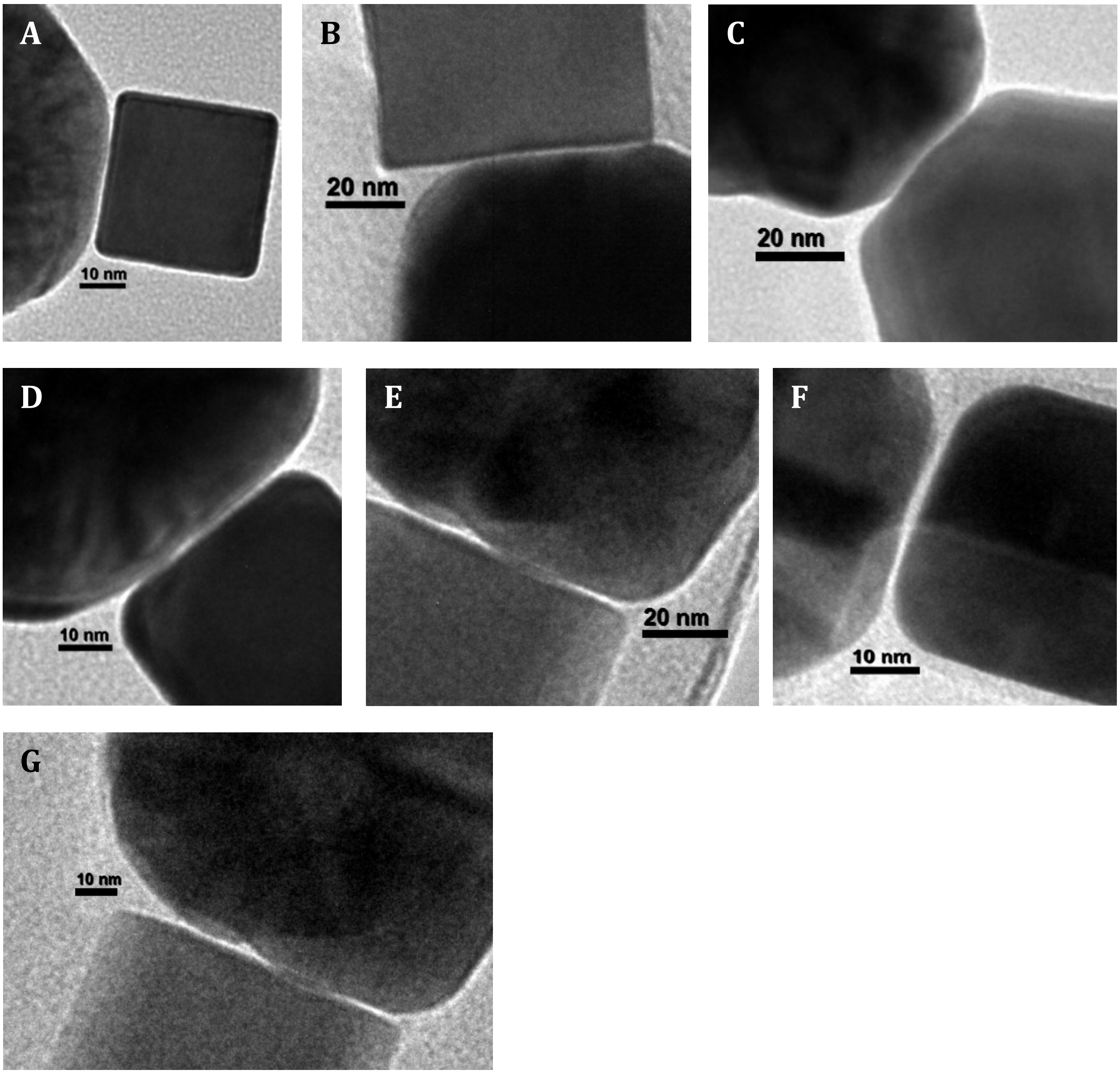

Figure SI8-1. Representative TEM images used for the determination of interparticle gaps: A) Au 90 nm- Pd 25 nm; B) Au 90 nm- Pd 70 nm; C) Au 90 nm, Au rhombic; D) Au 90 nm, Au cube; E) Ag 90 nm- Pd 70 nm; F) Ag 90 nm- Au cube; G) Ag 90 nm – Pd 70 nm.

SI-9: References for supporting information

(1) Wu, H.-L.; Kuo, C.-H.; Huang, M. H. Seed-Mediated Synthesis of Gold Nanocrystals with Systematic Shape Evolution from Cubic to Trisoctahedral and Rhombic Dodecahedral Structures. *Langmuir* **2010**, *26*, 12307–12313.

(2) Niu, W.; Li, Z.-Y.; Shi, L.; Liu, X.; Li, H.; Han, S.; Chen, J.; Xu, G. Seed-Mediated Growth of Nearly Monodisperse Palladium Nanocubes with Controllable Sizes. *Cryst. Growth Des.* **2008**, *8*, 4440–4444.

(3) Niu, W.; Zhang, L.; Xu, G. Shape-Controlled Synthesis of Single-Crystalline Palladium Nanocrystals. *ACS Nano* **2010**, *4*, 1987–1996.

(4) Hogg, B. Y. R.; Healy, T. W.; Fuerstenau, D. W. Mutual Coagulation of Colloidal Dispersions. *Trans. Faraday Soc.* **1966**, *33*, 1638–1651.

(5) Lee, K.; Sathyagal, A. N.; McCormick, A. V. A Closer Look at an Aggregation Model of the Stöber Process. *Colloids Surf.* **1998**, *144*, 115–125.

(6) Kim, T.; Lee, C.-H.; Joo, S.-W.; Lee, K. Kinetics of Gold Nanoparticle Aggregation: Experiments and Modeling. *J. Colloid Interface Sci.* **2008**, *318*, 238–243.

(7) Ohshima, H. Effective Surface Potential and Double-Layer Interaction of Colloidal Particles. *J. Colloid Interface Sci.* **1995**, *174*, 45–52.

(8) Ohshima, H. Surface Charge Density/surface Potential Relationship for a Spherical Colloidal Particle in a Salt-Free Medium. *J. Colloid Interface Sci.* **2002**, *247*, 18–23.

(9) Barzykin, A. V. Statistical Mechanical Treatment of a Compartmentalized Molecular Ensemble. Application to Electronic Energy Transfer in Micellar Systems. *Chem. Phys.* **1992**, *161*, 63–76.